

Quantum simulation for three-dimensional chiral topological insulator

Wentao Ji^{1,2,5*}, Lin Zhang^{3,4*}, Mengqi Wang^{1,2,5}, Long Zhang^{3,4},
 Yuhang Guo^{1,2,5}, Zihua Chai^{1,2,5}, Xing Rong^{1,2,5}, Fazhan Shi^{1,2,5},
 Xiong-Jun Liu^{3,4,6,7†}, Ya Wang^{1,2,5†}, Jiangfeng Du^{1,2,5†}

¹ Hefei National Laboratory for Physical Sciences at the Microscale and
 Department of Modern Physics,

University of Science and Technology of China (USTC), Hefei, 230026, China.

² CAS Key Laboratory of Microscale Magnetic Resonance, USTC, Hefei, 230026, China.

³ International Center for Quantum Materials, School of Physics,
 Peking University, Beijing 100871, China.

⁴ Collaborative Innovation Center of Quantum Matter, Beijing 100871, China.

⁵ Synergetic Innovation Center of Quantum Information and Quantum Physics,
 USTC, Hefei, 230026, China.

⁶ Shenzhen Institute for Quantum Science and Engineering and Department of Physics,
 Southern University of Science and Technology, Shenzhen 518055, China.

⁷ Beijing Academy of Quantum Information Science, Beijing 100193, China

* These authors contributed equally to this work.

† E-mail: xiongjunliu@pku.edu.cn, ywustc@ustc.edu.cn, djf@ustc.edu.cn

April 28, 2022

One Sentence Summary: A complete simulation of the bulk and surface topological physics of the three-dimensional chiral topological insulator is demonstrated.

Quantum simulation, as a state-of-art technique, provides the powerful way to explore topological quantum phases beyond natural limits. Nevertheless,

a complete simulation of the bulk and surface topological physics, and their correspondence is usually hard to achieve in one single simulator. Here we build up a quantum simulator using nitrogen-vacancy center to investigate a previously-not-realized three-dimensional (3D) chiral topological insulator, and demonstrate by quantum quenches a complete study of both the bulk and surface topological physics. First, a dynamical bulk-surface correspondence in momentum space is observed, showing that the bulk topology of the 3D phase uniquely corresponds to the nontrivial quench dynamics emerging on 2D momentum hypersurfaces called band inversion surfaces (BISs), equivalent to the bulk-boundary correspondence in real space. Further, the symmetry protection of the 3D chiral phase is uncovered by measuring dynamical spin textures on BISs, which exhibit perfect (broken) topology when the chiral symmetry is preserved (broken). Finally we measure the topological charges to characterize directly the bulk topology, and identify an emergent dynamical topological transition when varying the quenches from deep to shallow regimes. This work opens a new avenue of quantum simulation towards for the complete study of topological quantum phases.

INTRODUCTION

The past over one decade has witnessed the explosive progress in the field of topological quantum phases (1–3), with many exotic topological states having been discovered in the tabletop materials (4–6). The most prominent classes of topological materials include the time-reversal invariant topological insulators (7–10), quantum anomalous Hall insulators (11), topological semimetals (12–14), and topological superconductors (15–17). These topological phases are characterized by nontrivial topology in the bulk, and host topology- or symmetry-protected

gapless boundary modes which are connected to the bulk through the bulk-boundary correspondence (1–3). Such bulk-boundary correspondence has been the dominant mechanism for the observation of the topological states, with most topological materials having been uncovered in experiment by resolving the boundary physics (8, 9, 13, 14), while the bulk topology, however, is hard to be directly measured for solid systems.

Despite the considerable achievements, only a small portion of the broad classes of topological phases predicted in theory have been observed in condensed matter physics (18–20). Quantum simulation (21), as a state-of-art technique, provides a powerful way to explore exotic quantum phases beyond natural limits (22). A number of exotic quantum systems, such as the two-dimensional (2D) Haldane model (23) and 2D spin-orbit (SO) coupled minimal model for quantum anomalous Hall phase (24–26), 1D chiral topological phase (27–30), and 3D semimetals (31, 32) have been successfully realized in a controllable fashion with various quantum simulators including the ultracold atoms (33), photonic crystals (34, 35), and solid-state qubit systems (36). Nevertheless, in these studies, either the bulk or only the boundary physics of the simulated topological states can be well explored. For example, in ultracold atoms, it is convenient to measure the bulk topology but hard to simulate the boundary (23, 25, 26, 37, 38). Therefore, a complete study of both the bulk and boundary topological physics, and their correspondence is challenging for quantum simulators.

In this work, we build up a quantum simulator using nitrogen-vacancy (NV) center to investigate 3D chiral topological insulator which was not accessible in solid systems, and demonstrate a complete study of the bulk and surface topological physics of the simulated chiral phase. This study is based on the recently proposed dynamical bulk-surface correspondence in momentum space (41–48), which bridges the bulk topology of a d D equilibrium phase and the nontrivial quench dynamics emerging on $(d-1)$ D momentum hypersurfaces called band inversion surfaces (BISs). The dynamical bulk-surface correspondence resembles the bulk-boundary

correspondence in real space, and is easier to emulate than the latter, since the momentum space can be readily engineered for quantum simulators. This facilitates complete studies of the simulated topological phases. In demonstrating the correspondence between the bulk and surface topological physics, we show in experiment the chiral symmetry protection of the 3D topological phase, and further measure the topological charges to directly characterize the bulk topology, with an emergent dynamical topological transition being observed.

RESULTS

Simulation of the 3D model

The 3D chiral topological insulator simulated in the current experiment is described by the Bloch Hamiltonian $\mathcal{H}_{3D}(\mathbf{k}) = \sum_{j=0}^4 h_j \gamma_j$ as

$$\begin{aligned} \mathcal{H}_{3D}(\mathbf{k}) = & [m_z - t_0(\cos k_x + \cos k_y + \cos k_z)] \gamma_0 \\ & + t_{so}(\sin k_x \gamma_1 + \sin k_y \gamma_2 + \sin k_z \gamma_3), \end{aligned} \quad (1)$$

where the Bloch momentum $\mathbf{k} = (k_x, k_y, k_z)$, the Dirac matrices $\gamma_0 = \sigma_z \otimes \tau_z$, $\gamma_1 = \sigma_x \otimes \mathbf{1}$, $\gamma_2 = \sigma_y \otimes \mathbf{1}$, and $\gamma_3 = \sigma_z \otimes \tau_x$, with the Pauli matrices $\sigma_{x,y,z}$ and $\tau_{x,y,z}$ in the present simulator corresponding to the electron and nuclear spins, respectively. The $h_0(\mathbf{k})$ -term with the parameters m_z and t_0 characterizes the dispersion of four uncoupled bands. The remaining part, written as $\mathbf{h}_{so}(\mathbf{k}) = (h_1, h_2, h_3)$, represents a spin-orbit field which couples the four different bands, with t_{so} simulating the spin-flipped hopping coefficient. The Hamiltonian has a chiral symmetry defined by $\gamma_4 = \sigma_z \otimes \tau_y$, hence it belongs to AIII class according to the Altland-Zirnbauer ten-fold symmetry classification (3, 49) and is characterized by 3D winding numbers in the equilibrium theory. The topological phases include three nontrivial regions: (i) $t_0 < m_0 < 3t_0$ with winding number $\nu_3 = 1$; (ii) $-t_0 < m_0 < t_0$ with $\nu_3 = -2$; and (iii) $-3t_0 < m_0 < -t_0$ with $\nu_3 = 1$. Beyond these regions the phase is trivial, and across the phase transition points

the bulk gap is closed.

We realize the Hamiltonian \mathcal{H}_{3D} by a quantum simulator built from NV center in diamond (50). The electrons around the center form an effective electron spin with a triplet ground state ($S = 1$). Together with the intrinsic nitrogen-14 nuclear spin ($I = 1$), it forms a coupled system, as depicted in Fig. 1(a). The Hamiltonian of the NV center is

$$\mathcal{H}_{\text{NV}} = 2\pi(DS_z^2 + \omega_e S_z + QI_z^2 + \omega_n I_z + AS_z I_z), \quad (2)$$

where S_z (I_z) denotes the electron (nuclear) spin operator, $D = 2.87\text{GHz}$ is the electronic zero-field splitting, $Q = -4.95\text{MHz}$ is the nuclear quadrupolar interaction, and $A = -2.16\text{MHz}$ is the hyperfine interaction. A magnetic field of 514G is applied along the NV's symmetry axis, yielding an electron (nuclear) Zeeman splitting ω_e (ω_n) of 1439 MHz (154 kHz). The subspace of $\{m_s = 0, -1\} \otimes \{m_i = +1, 0\}$ is utilized to form a two-qubit system, relabeled as $\{|0\rangle, |1\rangle\} \otimes \{|0\rangle, |1\rangle\}$, on which the Pauli operators σ_i and τ_i are defined. A microwave pulse is applied to produce an external driving field Ω_{mw} . Under the rotating-wave approximation, the effective Hamiltonian capturing the couplings in the subspace reads $\mathcal{H}_{mw, \text{RWA}} = 2\pi \left(\frac{A}{4} \sigma_z \tau_z + \Omega_x \sigma_x + \Omega_y \sigma_y \right)$, with $\Omega_x = \Omega_{mw} \cos \phi$ and $\Omega_y = -\Omega_{mw} \sin \phi$, where ϕ is the phase of microwave pulse. Finally, the $\sigma_z \tau_x$ term can be generated via a unitary rotation about τ_y axis by θ angle, yielding

$$\mathcal{H}_{\text{eff}} = \frac{A}{4} \cos \theta \sigma_z \tau_z + \Omega_x \sigma_x + \Omega_y \sigma_y + \frac{A}{4} \sin \theta \sigma_z \tau_x, \quad (3)$$

where the factor 2π is neglected. This τ_y -rotation of the Hamiltonian is realized by applying a radio-frequency pulse to rotate the nuclear spin. The experiment was performed on a home-built confocal setup at room temperature. We use a [111] oriented NV center with solid immersion lens. The MW and radio-frequency control of NV center are realized through an arbitrary wave generator.

The 3D chiral topological insulator model \mathcal{H}_{3D} can be emulated by \mathcal{H}_{eff} after mapping the parameter space to Bloch momentum space, i.e. $(\theta, \phi, \Omega_{mw}) \rightarrow \mathbf{k}$. Any state evolving under \mathcal{H}_{eff} is then mapped to the one evolving under \mathcal{H}_{3D} (51). Thus the \mathbf{k} -space of the 3D chiral phase can be fully engineered, while the real space including the boundary cannot be simulated for the quantum simulator. The key observation is that, as studied below, the dynamical bulk-surface correspondence in momentum space provides the alternative full investigation of the bulk and surface topological physics.

Dynamical bulk-surface correspondence

We present the nontrivial quench dynamics emerging on BISs and connected to the bulk topology. The experimental procedure for quench along γ_i axis consists of three steps [see Fig. 1(b)]. First, we initialize the state to the state $|00\rangle$, which is then prepared to be fully (or incompletely) polarized along γ_i axis by a unitary control. Then, the initialized state evolves by time t under \mathcal{H}_{3D} , as simulated by \mathcal{H}_{eff} , rendering the quench dynamics. Finally, we measure the spin polarization $\langle \gamma_j(t) \rangle$. The opposite unitary operations are respectively used to perform the quench and measurement with respect to all the spin components [Fig. 1(c)]. Following the measurement, we obtain the time-averaged spin polarizations $\overline{\langle \gamma_j \rangle}_i = \lim_{T \rightarrow \infty} (1/T) \int_0^T \langle \gamma_j(t) \rangle_i dt \propto h_i h_j$, which are key ingredients to characterize the topology (41). Here the index i (j) denotes the quench (measurement) axis.

The dynamical bulk-surface correspondence states that the bulk topology of the 3D chiral topological phase uniquely corresponds to the nontrivial quench dynamics emerging on the 2D BISs (41). For the initial state fully polarized in the axis γ_0 , the 2D BISs are formed by all the momenta points where spin oscillations are *resonant* and easily measurable, giving the vanishing time-averaged spin-polarizations

$$\text{BIS} = \{\mathbf{k} | \overline{\langle \gamma_i(\mathbf{k}) \rangle}_0 = 0, i = 0, 1, 2, 3\}. \quad (4)$$

A dynamical invariant can be defined on the BISs as the winding of an emergent dynamical spin-texture field $\mathbf{g}(\mathbf{k})$, with the i -th component $g_i(\mathbf{k}) = \frac{1}{\mathcal{N}_k} \partial_{k_\perp} \overline{\langle \gamma_i \rangle}_0|_{\mathbf{k} \in \text{BIS}}$ describing the variation slope of $\overline{\langle \gamma_i \rangle}_0$ along the local direction k_\perp perpendicular to the BISs and normalized by \mathcal{N}_k , and

$$\mathcal{W} = \frac{1}{8\pi} \int_{\text{BIS}} d^2\mathbf{k} \mathbf{g} \cdot (\nabla \mathbf{g} \times \nabla \mathbf{g}), \quad (5)$$

Geometrically, the dynamical invariant describes the coverage of the dynamical field $\mathbf{g}(\mathbf{k})$ over a 2D spherical surface. This dynamical topological invariant equals the bulk topological invariant of the ground band of \mathcal{H}_{3D} , and provides the dynamical characterization of the 3D chiral phase (41).

We show the experimental measurements of the three different topological regimes in Fig. 1(d-f). The BISs are measured and exhibit very different shapes in different phases. The measured dynamical field $\mathbf{g}(\mathbf{k})$ is depicted as arrows, from which with the 2D dynamical invariant \mathcal{W} can be computed, and is verified to characterize the 3D bulk topology.

Measuring the chiral symmetry protection

The dynamical bulk-surface correspondence is protected by the chiral symmetry. It is important to verify the symmetry protection by studying the symmetry-breaking effect on the quench dynamics on BISs, similar to the symmetry-breaking in the boundary states in real space. We create a constant term $h_4 \gamma_4 = h_4 \sigma_z \tau_y$ into \mathcal{H}_{3D} to break the chiral symmetry via an additional rotation in the τ_x axis. Then the dynamical spin-texture field on BISs becomes a 4D vector $\mathbf{g}(\mathbf{k}) = (g_1, g_2, g_3, g_4)$ with $g_i = \partial_{k_\perp} \overline{\langle \gamma_i \rangle}_0 / \mathcal{N}_k$, which locates on a 3D spherical surface S^3 . To quantify the geometric property of $\mathbf{g}(\mathbf{k})$, we note that without symmetry-breaking, i.e. $h_4 = 0$, the dynamical field $\mathbf{g}(\mathbf{k})$ sits on the equator of S^3 (equivalent to S^2). The solid angle enclosed by $\mathbf{g}(\mathbf{k})$ is a multiple of the half 3-sphere area, characterizing the invariant which can be gener-

alized to the symmetry breaking case as

$$\mathcal{W}_{\text{SB}} = \frac{1}{\pi^2} \int_{\mathcal{S}|\partial\mathcal{S}=\mathbf{g}(\mathbf{k})} dS^3, \quad (6)$$

where π^2 is the area of the half unit 3-sphere, dS^3 is the corresponding area element, and the integral is performed over the region \mathcal{S} with boundary $\partial\mathcal{S} = \mathbf{g}(\mathbf{k})$ (51).

The experimental measurement of the symmetry breaking effect is shown in Fig. 2. It is observed that once $h_4 \neq 0$, the 4D dynamical field $\mathbf{g}(\mathbf{k})$ is shifted away from the equator of S^3 , with a nonzero polarization in the γ_4 axis, for which the value $\mathcal{W}_{\text{SB}} \neq \mathcal{W}$ is no longer quantized and decreases with the strength h_4 . The results show that the symmetry protection of the bulk topological phase can be identified from the the dynamical spin textures on BISs, which exhibit perfect (broken) topology and zero (nonzero) γ_4 -polarization when the chiral symmetry is preserved (broken), similar to the boundary modes in real space which can be gapped out and polarized by the symmetry-breaking term.

Topological charges and emergent dynamical transition

We proceed to detect topological charges and characterize directly the bulk topology by the total charges enclosed by BISs (43), which further demonstrates the correspondence between the bulk and surface topological physics. In this case, instead of measuring all spin components after a single quench along γ_0 , we perform a series of quantum quenches along different γ_i ($i = 0, 1, 2, 3$) axes but measure only γ_0 component, i.e. $\overline{\langle \gamma_0(\mathbf{k}) \rangle}_i$ after each quench (43, 44). To realize quenches in different axes γ_i , the quench process [see Fig. 1(c)] is modified to an appropriate combination of the nuclear and electron spin rotations, such that the resulting initial state is the eigenstate of the pre-quench Hamiltonian $\mathcal{H}_{\text{pre}} = m_i \gamma_i + \mathcal{H}_{3D}$ (51). The BISs are again the collection of momenta on which time-averaged spin polarizations all vanish, namely $\text{BIS} = \{\mathbf{k} | \overline{\langle \gamma_0(\mathbf{k}) \rangle}_i = 0, \forall i\}$, and the locations of topological charges are determined

by $\overline{\langle \gamma_0(\mathbf{k}) \rangle}_{1,2,3} = 0$ while $\overline{\langle \gamma_0(\mathbf{k}) \rangle}_0 \neq 0$ (43). The topological charge is characterized by the dynamical field $\Theta(\mathbf{k})$ with components ($i = 1, 2, 3$)

$$\Theta_i(\mathbf{k}) \equiv \frac{\text{sgn}(h_0(\mathbf{k}))}{\mathcal{N}_k} \overline{\langle \gamma_0(\mathbf{k}) \rangle}_i. \quad (7)$$

The norm of $\Theta(\mathbf{k})$ vanishes at a charge, and the charge value equals the winding of the dynamical field $\Theta(\mathbf{k})$ near the charge. In Fig. 3(a), we measure the norm of $|\Theta(\mathbf{k})|$ on the $k_z = 0, -\pi$ and $k_x = 0, -\pi$ planes for the phase with $m_z = 1.4t_0$ and $t_{\text{so}} = t_0$, which shows eight topological charges O_i in the bulk. The dynamical field $\Theta(\mathbf{k})$ near the charges is shown in Fig. 3(b) and (c), showing that the topological charges $O_{1,3,5,7}$ have value $+1$ while the charges $O_{2,4,6,8}$ have value -1 . The bulk topology is characterized by the total topological charge enclosed by the BIS [see Fig. 3(a)], which is O_1 , giving $\nu_3 = +1$ for the bulk phase [Fig. 1(d)].

An interesting observation of the dynamical characterization with topological charges is that an emergent dynamical topological transition occurs when the quenches are varied from deep to shallow regimes (44). The deep (shallow) quench regime corresponds to large (small) m_i , and the initial state is fully (partially) polarized in the axis γ_i , independent of (dependent on) \mathbf{k} . For simplicity, in each set of quenches we take the same m_i when quenching in different axes. The BISs are not affected by the quench depth m_i (44). To characterize the emergent topological transition we measure the dynamical field $\mathbf{f}(\mathbf{k})$ on BISs, with components given by

$$f_i(\mathbf{k}) = \frac{1}{\mathcal{N}_k} \partial_{k_\perp} \overline{\langle \gamma_0 \rangle}_i \Big|_{\mathbf{k} \in \text{BIS}}, \quad (8)$$

with $i = 1, 2, 3$. For deep quenches, $\mathbf{f}(\mathbf{k})$ is equivalent to $\mathbf{g}(\mathbf{k})$, whose winding on BISs characterizes the post-quench topology [see the right insert in Fig. 4(a)]. In the left insert of Fig. 4(a), we show that the dynamical field $\mathbf{f}(\mathbf{k})$ for shallow quenches with $m_i = 2$ is deformed and has zero winding, implying that between deep and shallow quenches an emergent topological transition occurs. To determine the critical quench depth m_c , we notice that the dynamical field changes most dramatically near the momentum \mathbf{k}_0 on the BIS in the $[\bar{1}\bar{1}\bar{1}]$ direction. In reducing

m_i across m_c , the direction of $\mathbf{f}(\mathbf{k}_0)$ changes from the outward to inward of BIS, and vanishes at $m_i = m_c$, where the winding on BIS is ill-defined. Fig. 4(a) displays the projection of $\mathbf{f}(\mathbf{k}_0)$ in the $\overline{[111]}$ direction. Our measurement determines the critical value $m_c \simeq 2.7t_0$, which agrees on the theoretical prediction $m_c = 2.653t_0$.

The dynamical topological transition corresponds to the movement of topological charges across BIS, as illustrated in Fig. 4(b). The dynamical field $\Theta(\mathbf{k})$ is measured along the line connecting charges O_1 - O_8 or O_3 - O_6 . We observe that the locations of charges depend on the quench depth m_i . Particularly, the charge O_8 passes through BIS when reducing m_i across the critical value m_c . Then no topological charge is enclosed by the BIS, providing the alternative picture of the emergent topological transition. The topological charges O_3 and O_6 can also annihilate at certain m_i , but do not change the dynamical topology on the BIS.

Conclusion

In summary, we have achieved by quantum quenches a complete simulation of bulk and surface topological physics for a novel 3D chiral topological insulator, using a quantum simulator built from solid-state spin system. We experimentally identified the dynamical bulk-surface correspondence in momentum space, as a momentum-space counterpart of the bulk-boundary correspondence in real space, which bridges the bulk topology of the 3D chiral phase and the nontrivial quench dynamics emerging on 2D band inversion surfaces. As the momentum space is more convenient to engineer for quantum simulators, the dynamical bulk-surface correspondence enables a study of the simulated topological phases, without the necessity of constructing real-space boundaries. The novel topological physics have been observed in experiment, including the chiral symmetry protection, the topological charges, and the dynamical topological transition emerging in the quench studies. The present work showed the insightful techniques of quantum simulation, which can be easily extended to other simulators, and opens a broad

avenue to explore high dimensional topological phases beyond the limits of condensed matter physics.

Acknowledgements

Funding: This work is supported by the National Key R&D Program of China (Grant No. 2018YFA0306600, 2017YFA0305000, 2016YFA0301604, 2016YFB0501603), the NNSFC (Grants No. 11775209, 11825401, 81788101, 11761161003, 11921005, 11761131011, 11722544), the CAS (Grants No. GJJSTD20170001, No. QYZDY-SSW-SLH004, No. QYZDB-SSW-SLH005), Anhui Initiative in Quantum Information Technologies (Grant No. AHY050000), the Fundamental Research Funds for the Central Universities, the Thousand-Young-Talent Program of China. **Author contributions:** J.D.supervised the project; X.-J.L., Y.W. and J.D. conceived the ideas; L.Z. and X.-J.L. formulated the theory; Y.W. supervised the experiments; W.T.J., M.Q.W. Y.G. and Z.H.C. prepared the sample and performed the experiments; W.T.J. and L.Z. wrote the manuscript with input from all authors. All authors along reviewed the manuscript and suggested improvements. **Competing Interests:** All authors declare that they have no competing interests. **Data and materials availability:** All data needed to evaluate the conclusions in the paper are present in the paper and/or the Supplementary Materials. Additional data related to this paper may be requested from the authors.

References

1. M. Z. Hasan and C. L. Kane, Rev. Mod. Phys. **82**, 3045 (2010).
2. X.-L. Qi and S.-C. Zhang, Rev. Mod. Phys. **83**, 1057 (2011).
3. C.-K. Chiu, J. C. Y. Teo, A. P. Schnyder, and S. Ryu, Rev. Mod. Phys. **88**, 035005 (2016).
4. B. Yan and S.-C. Zhang, Rep. Prog. Phys. **75**, 096501 (2012).

5. Y. Ando, *J. Phys. Soc. Jpn.* **82**, 102001 (2013).
6. B. Yan and C. Felser, *Annu. Rev. Condens. Matter Phys.* **8**, 337 (2017).
7. M. König, S. Wiedmann, C. Brüne, A. Roth, H. Buhmann, L. W. Molenkamp, X.-L. Qi, and S.-C. Zhang, *Science* **318**, 766 (2007).
8. D. Hsieh, D. Qian, L. Wray, Y. Xia, Y. S. Hor, R. J. Cava, and M. Z. Hasan, *Nature* **452**, 970 (2008).
9. Y. Xia, D. Qian, D. Hsieh, L. Wray, A. Pai, H. Lin, A. Bansil, D. Grauer, Y. S. Hor, R. Cave, and M. Hasan, *Nat. Phys.* **5**, 398 (2009).
10. I. Knez, R.-R. Du, and G. Sullivan, *Phys. Rev. Lett.* **107**, 136603 (2011).
11. C.-Z. Chang, J. Zhang, X. Feng, J. Shen, Z. Zhang, M. Guo, K. Li, Y. Ou, P. Wei, L.-L. Wang, Z.-Q. Ji, Y. Feng, S. Ji, X. Chen, J. Jia, X. Dai, Z. Fang, S.-C. Zhang, K. He, Y. Wang, L. Lu, X.-C. Ma, and Q.-K. Xue, *Science* **340**, 167 (2013).
12. Z. K. Liu, B. Zhou, Y. Zhang, Z. J. Wang, H. M. Weng, D. Prabhakaran, S.-K. Mo, Z. X. Shen, Z. Fang, X. Dai, Z. Hussain, and Y. L. Chen, *Science* **343**, 864 (2014).
13. B. Q. Lv, H. M. Weng, B. B. Fu, X. P. Wang, H. Miao, J. Ma, P. Richard, X. C. Huang, L. X. Zhao, G. F. Chen, Z. Fang, X. Dai, T. Qian, and H. Ding, *Phys. Rev. X* **5**, 031013 (2015).
14. S.-Y. Xu, I. Belopolski, N. Alidoust, M. Neupane, G. Bian, C. Zhang, R. Sankar, G. Chang, Z. Yuan, C.-C. Lee, S.-M. Huang, H. Zheng, J. Ma, D. S. Sanchez, B. Wang, A. Bansil, F. Chou, P. P. Shibayev, H. Lin, S. Jia, and M. Z. Hasan, *Science* **349**, 613 (2015).

15. V. Mourik, K. Zuo, S. M. Frolov, S. R. Plissard, E. P. A. M. Bakkers, and L. P. Kouwenhoven, *Science* **336**, 1003 (2012).
16. H.-H. Sun, K.-W. Zhang, L.-H. Hu, C. Li, G.-Y. Wang, H.-Y. Ma, Z.-A. Xu, C.-L. Gao, D.-D. Guan, Y.-Y. Li, C. Liu, D. Qian, Y. Zhou, L. Fu, S.-C. Li, F.-C. Zhang, and J.-F. Jia, *Phys. Rev. Lett.* **116**, 257003 (2016).
17. P. Zhang, K. Yaji, T. Hashimoto, Y. Ota, T. Kondo, K. Okazaki, Z. Wang, J. Wen, G. D. Gu, H. Ding, and S. Shin, *Science* **360**, 182 (2018).
18. T. Zhang, Y. Jiang, Z. Song, H. Huang, Y. He, Z. Fang, H. Weng, and C. Fang, *Nature* **566**, 475 (2019).
19. M. G. Vergniory, L. Elcoro, C. Felser, N. Regnault, B. A. Bernevig, and Z. Wang, *Nature* **566**, 480 (2019).
20. F. Tang, H. C. Po, A. Vishwanath, and X. Wan, *Nature* **566**, 486 (2019).
21. R. Feynman, *Int. J. Theor. Phys.* **21**, 467 (1982).
22. I. M. Georgescu, S. Ashhab, and F. Nori, *Rev. Mod. Phys.* **86**, 153 (2014).
23. G. Jotzu, M. Messer, R. Desbuquois, M. Lebrat, T. Uehlinger, D. Greif, and T. Esslinger, *Nature* **515**, 237 (2014).
24. X.-J. Liu, K. T. Law, and T. K. Ng, *Phys. Rev. Lett.* **112**, 086401 (2014).
25. Z. Wu, L. Zhang, W. Sun, X.-T. Xu, B.-Z. Wang, S.-C. Ji, Y. Deng, S. Chen, X.-J. Liu, and J.-W. Pan, *Science* **354**, 83 (2016).
26. W. Sun, B.-Z. Wang, X.-T. Xu, C.-R. Yi, L. Zhang, Z. Wu, Y. Deng, X.-J. Liu, S. Chen, and J.-W. Pan, *Phys. Rev. Lett.* **121**, 150401 (2018).

27. M. Atala, M. Aidelsburger, J. T. Barreiro, D. Abanin, T. Kitagawa, E. Demler, and I. Bloch, *Nat. Phys.* **9**, 795 (2013).

28. X.-J. Liu, Z.-X. Liu, and M. Cheng, *Phys. Rev. Lett.* **110**, 076401 (2013).

29. B. Song, L. Zhang, C. He, T. F. J. Poon, E. Hajiiev, S. Zhang, X.-J. Liu, and G.-B. Jo, *Sci. Adv.* **4**, aao4748 (2018).

30. D. Xie, T.-S. Deng, T. Xiao, W. Gou, T. Chen, W. Yi, and B. Yan, *Phys. Rev. Lett.* **124**, 050502 (2019).

31. B. Song, C. He, S. Niu, L. Zhang, Z. Ren, X.-J. Liu, and G.-B. Jo, *Nat. Phys.* **15**, 911 (2019).

32. X. Tan, Y. X. Zhao, Q. Liu, G. Xue, H.-F. Yu, Z. D. Wang, and Y. Yu, *Phys. Rev. Lett.* **122**, 010501 (2019).

33. I. Bloch, J. Dalibard, and S. Nascimbene, *Nat. Phys.* **8**, 267 (2012).

34. A. Aspuru-Guzik, and P. Walther, *Nat. Phys.* **8**, 285 (2012).

35. L. Lu, J.D. Joannopoulos, and M. Soljačić, *Nat. Photonics* **8**, 821 (2014).

36. A. A. Houck, H. E. Türeci, and J. Koch, *Nat. Phys.* **8**, 292 (2012).

37. M. Aidelsburger et al., Measuring the Chern number of Hofstadter bands with ultracold bosonic atoms. *Nat. Phys.* **11**, 162 (2015).

38. A synthetic boundary can be simulated with the synthetic dimension formed by internal degree of freedom, e.g. the hyperfine levels of ultracold atoms (39, 40).

39. M. Mancini et al., Observation of chiral edge states with neutral fermions in synthetic Hall ribbons. *Science* **349**, 1510 (2015).

40. B. K. Stuhl, H.-I. Lu, L. M. Aycock, D. Genkina, and I. B. Spielman, Visualizing edge states with an atomic 372 Bose gas in the quantum Hall regime. *Science* **349**, 1514 (2015).

41. L. Zhang, L. Zhang, S. Niu, and X.-J. Liu, *Sci. Bull.* **63**, 1385 (2018).

42. L. Zhang, L. Zhang, Y. Hu, S. Niu, and X.-J. Liu, arXiv:1903.09144.

43. L. Zhang, L. Zhang, and X.-J. Liu, *Phys. Rev. A* **99**, 053606 (2019).

44. L. Zhang, L. Zhang, and X.-J. Liu, *Phys. Rev. A* **100**, 063624 (2019).

45. L. Zhou and J. Gong, *Phys. Rev. B* **98**, 205417 (2018).

46. W. Sun, C.-R. Yi, B.-Z. Wang, W.-W. Zhang, B. C. Sanders, X.-T. Xu, Z.-Y. Wang, J. Schmiedmayer, Y. Deng, X.-J. Liu, S. Chen, and J.-W. Pan, *Phys. Rev. Lett.* **121**, 250403 (2018).

47. Y. Wang, W. Ji, Z. Chai, Y. Guo, M. Wang, X. Ye, P. Yu, L. Zhang, X. Qin, P. Wang, F. Shi, X. Rong, D. Lu, X.-J. Liu, and J. Du, *Phys. Rev. A* **100**, 052328 (2019).

48. C.-R. Yi, L. Zhang, L. Zhang, R.-H. Jiao, X.-C. Cheng, Z.-Y. Wang, X.-T. Xu, W. Sun, X.-J. Liu, S. Chen, and J.-W. Pan, *Phys. Rev. Lett.* **123**, 190603 (2019).

49. A. Altland and M. R. Zirnbauer, *Phys. Rev. B* **55**, 1142 (1997).

50. M. W. Doherty, N. B. Manson, P. Delaney, F. Jelezko, J. Wrachtrup, and L. C. L. Hollenberg, *Phys. Rep.* **528**, 1 (2013).

51. See Supplementary Material for details.

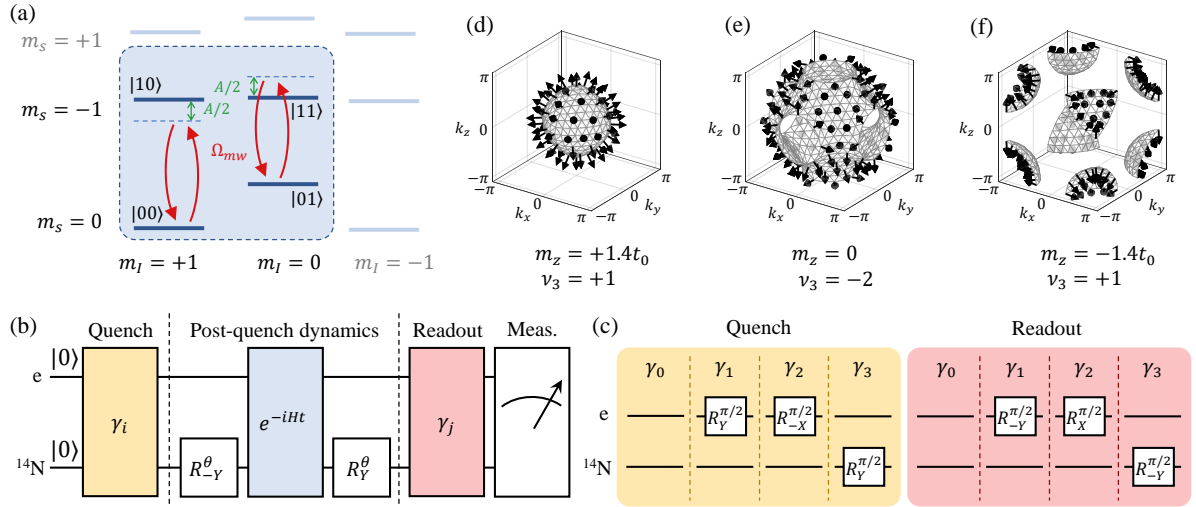


Figure 1: **Experimental scheme and the dynamical bulk-surface correspondence.** (a) The energy diagram of the NV center used for simulation. The electron and the nitrogen nuclear spins are used to form the two-qubit system. A microwave pulse is applied to simulate the 3D model. (b) Quantum circuit for the experiment. The operator e^{-iHt} corresponds to evolution under $\mathcal{H}_{mw,\text{RWA}}$, while the net effect together with the two nuclear spin operation $R_{\pm Y}^\theta$ is equivalent to evolution under \mathcal{H}_{eff} . (c) Operations of quench and readout steps in (b). (d-f) Experimental observation of the band inversion surfaces (BISs) and the dynamical spin-texture field $\mathbf{g}(\mathbf{k})$ (arrows) for $m_z = +1.4, 0$ and -1.4 , respectively. The winding of $\mathbf{g}(\mathbf{k})$ on BISs characterizes the 3D winding number v_3 . Here $t_{\text{so}} = 0.2t_0$.

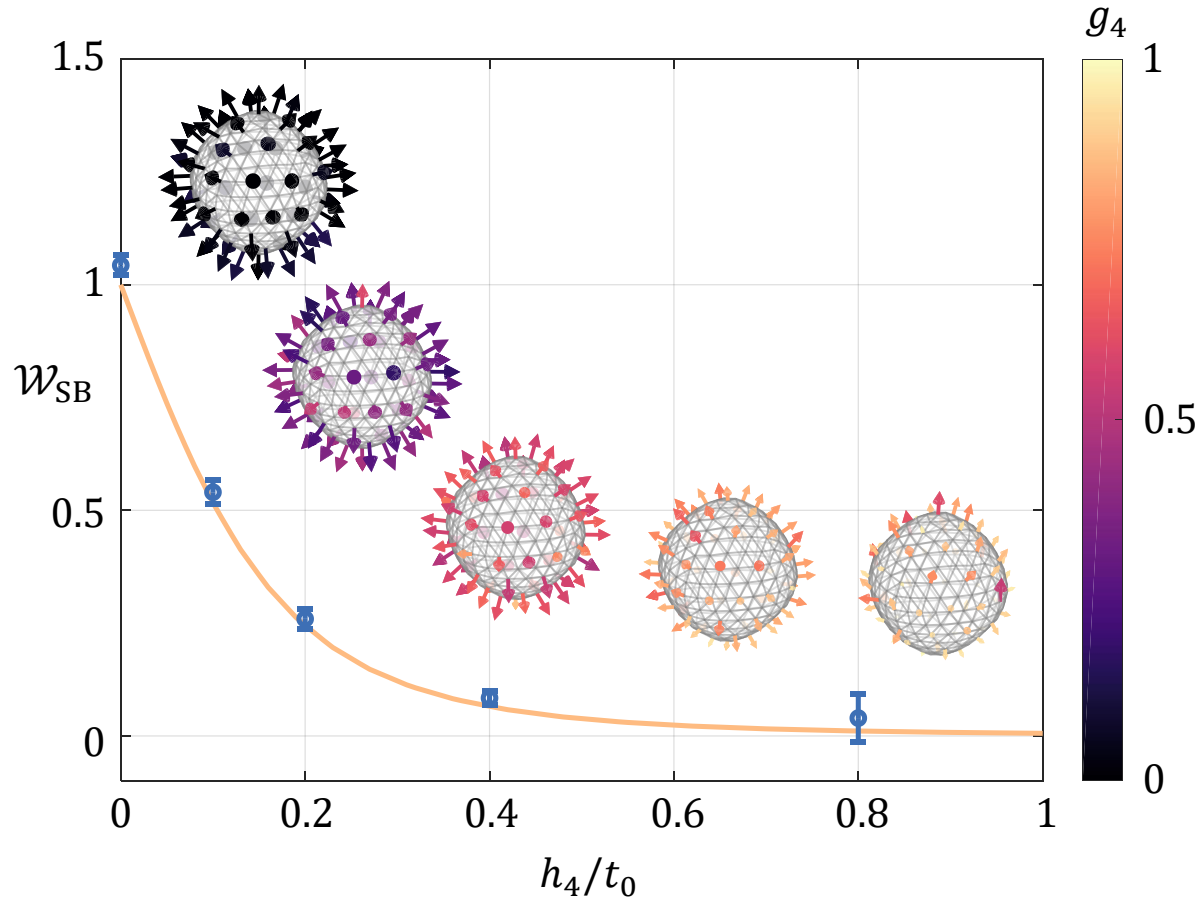


Figure 2: **Measuring the chiral symmetry protection.** The blue data points are experimental results of winding numbers obtained from the emergent dynamical spin-texture field, and the error-bars represent three standard deviation. The orange line is calculated from the theoretic model. The insets are the emergent dynamical spin-texture field $\mathbf{g}(\mathbf{k}) = (g_1, g_2, g_3, g_4)$ correspond to each data point. The arrows denote $g_{1,2,3}$ components, and the color of the arrows denotes the component g_4 .

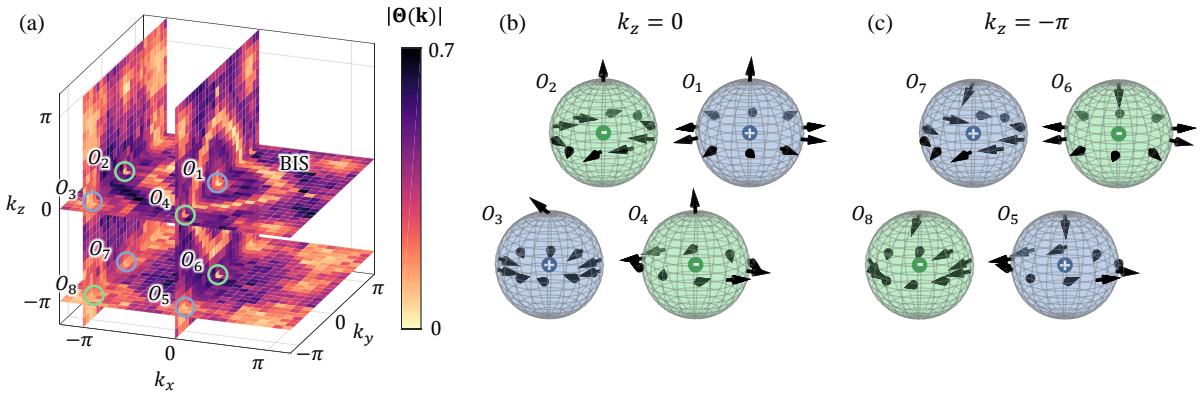


Figure 3: **Dynamical measurement of topological charges.** (a) Experimental results of the dynamical field $\Theta(\mathbf{k})$ constructed from $\langle \gamma_0(\mathbf{k}) \rangle_{1,2,3}$. The color of the pixels indicates the norm of $\Theta(\mathbf{k})$, which vanishes at the location of BIS and topological charges. The positive (negative) charges are marked out with blue (green) circles. (b)(c) Dynamical field $\Theta(\mathbf{k})$ at around the charges on $k_z = 0$ and $k_z = -\pi$ plane.

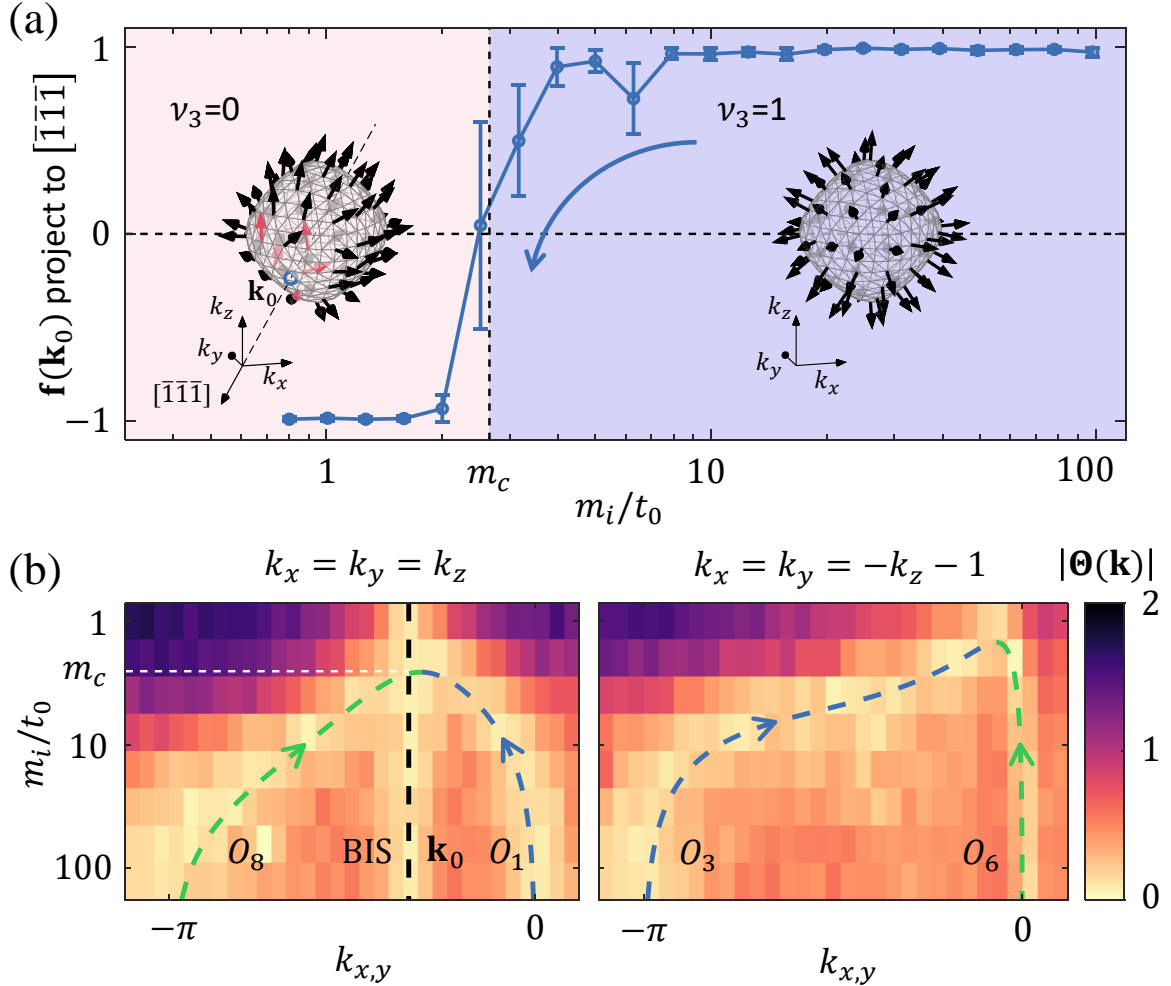


Figure 4: **Identifying dynamical topological transition.** (a) Experimental results of dynamical spin-texture field $\mathbf{f}(\mathbf{k}_0)$ projected onto $\bar{[111]}$ direction versus quench field. Here $k_{0x} = k_{0y} = k_{0z} = -1.084$ is the momentum on BIS in the $\bar{[111]}$ direction. The emergent topological transition point is around $m_c = 2.7t_0$. Insets are $\mathbf{f}(\mathbf{k})$ for a shallow quench (left inset, $m_i = 2t_0$) and a deep quench (right inset, $m_i = \infty$). At \mathbf{k}_0 point (blue circle) in the left inset, $\mathbf{f}(\mathbf{k})$ points inward the BIS (highlighted in red). (b) Locations of topological charges versus quench field. Dynamical field $\Theta(\mathbf{k})$ is measured along the line connecting charges O_1 - O_8 (left) and O_3 - O_6 (right), with the quench field m_i being varied. The charge O_8 cross the BIS at m_c and merges with O_1 .